Journal of Magnetic Resonance 301 (2019) 40–48

Contents lists available at ScienceDirect

Journal of Magnetic Resonance

journal homepage: www.elsevier.com/locate/jmr

Investigating pore geometry in heterogeneous porous samples using spatially resolved $G_0 - \Delta\chi_{app}$ and $G_0 - \Delta\nu$ correlations

Henrik Nicolay Sørgård *, John Georg Seland

University of Bergen, Department of Chemistry, Realfagsbygget, Allgaten 41, N-5007 Bergen, Norway

ARTICLE INFO

Article history:
Received 2 November 2018
Revised 21 February 2019
Accepted 28 February 2019
Available online 1 March 2019

Keywords:
NMR spectroscopy
Pore geometry

ABSTRACT

This study presents a two-dimensional NMR pulse sequence for obtaining spatially resolved correlations between magnetic susceptibility induced internal gradients (G_0), and both the apparent difference in magnetic susceptibility ($\Delta\chi_{app}$) and spectral frequency ($\Delta\nu$). $G_0 - \Delta\chi_{app}$ correlations were utilized to generate spatially resolved pore size distributions, while the $G_0 - \Delta\nu$ correlations were used to additionally evaluate sample heterogeneity. The spatially resolved measurements were performed on a water saturated heterogeneous porous sample which contains one layer of 5–50 μm glass spheres (top layer) and one layer of 140–165 μm glass spheres (bottom layer). The slice selection was validated by applying the pulse sequence on a liquid mineral oil and water sample as well as on the porous sample. The resulting spatially resolved pore size distributions show very good agreement with results from our previously published non slice selective pulse sequence in the 140–165 μm glass spheres and good agreement in the 5–50 μm glass spheres. The $G_0 - \Delta\nu$ correlations correctly indicate a slightly higher degree of heterogeneity in the 5–50 μm glass spheres compared to the 140–165 μm glass spheres.

1. Introduction

Introducing a fluid saturated porous sample to a homogeneous magnetic field B_0, can cause significant gradients to occur in the pore space. Such gradients are induced by the magnetic susceptibility difference $\Delta\chi$, between fluids and the matrix and are commonly named internal gradients G_0 [1–7]. The line broadening $\Delta\nu$, caused by the magnetic susceptibility difference in a porous sample, is related to the free induction decay (FID) time constant T_2^* [4,5,8]. In our samples it is assumed that susceptibility differences dominate T_2^*.

$$\Delta\nu \approx \frac{1}{\pi T_2^*} \approx \frac{\gamma}{2\pi} B_0 \Delta\chi_{app} \tag{1}$$

Apparent magnetic susceptibility difference $\Delta\chi_{app}$ is defined as $\Delta\chi_{app} = C\Delta\chi$, where C is a dimensionless constant which corrects for large local variations in the internal field [5,9]. As a first order approximation, the internal magnetic field B_i, is related to the internal gradient G_0 in a single pore, $\Delta\chi_{app}$ and the pore diameter a [1,3,8]. G_0 is assumed to remain constant over the length of the pore.

$$\nabla B_i \equiv G_0 \approx \frac{B_0 \Delta\chi_{app}}{a} \tag{2}$$

From examining Eq. (2) one can see that $G_0 - \Delta\chi_{app}$ correlations can probe the pore geometry. Our research group recently [8] showed that pore size distributions based on such correlations agree well with those obtained from the well established Decay due to Diffusion in the Internal Field (DDIF) [10] method. However, the DDIF and the $G_0 - \Delta\chi_{app}$ methods do not include spatial resolution which is of interest in porous media where the pore geometry varies across the sample.

Zhang et al. (2018) obtained spatially resolved pore size – T_2 correlations by expanding the DDIF method to include a Carr-Purcell-Meiboom-Gill (CPMG) train with frequency encoding on the resulting echoes in low field NMR [11]. However, the DDIF method is based on a stimulated echo created from three $\pi/2$ pulses. As internal gradients increases proportional to the external magnetic field, so does the rate of diffusion and the decoding time in the DDIF method must therefore be kept very short at high fields to maintain the correct diffusion regime. Refocusing and separating the stimulated echo of interest from the rest of the occurring echoes [12] in the DDIF method, and still remain inside the correct diffusion regime for liquids inside porous samples is therefore problematic at high magnetic field strengths. Spatial resolution through frequency encoding in the DDIF-T_2 method is thus challenging in high field NMR.

---

* Corresponding author.
E-mail address: Henrik.Sorgard@uib.no (H.N. Sørgård).

https://doi.org/10.1016/j.jmr.2019.02.008

Sun and Dunn (2002) introduced $G_0^2D - T_2$ correlations through a modified CPMG pulse sequence where G_0^2D was decoded during the first part of the sequence by varying the echo spacing over a constant time period. Zhang and Blümich (2015) extended this sequence to incorporate spatial resolution by frequency encoding the echoes occurring in the second part of the sequence (CPMG train). Zhang and Blümich found it possible to distinguish between oil and water using 2D $G_0^2D - T_2$ maps in glass bead samples.

Through computer simulations, it has been shown [13,14] that the edges of a spectrum (high absolute values of $\Delta\nu$) correspond to more confined liquid molecules. Burcaw and Callahan [14] also showed through experimental data that $G_0 - \Delta\nu$ correlations may be used to predict the degree of heterogeneity in a porous sample.

In this paper we continue our research group's previous work [8,15] and introduce a 2D pulse sequence to obtain slice selective $G_0 - \Delta\chi_{app}$ and $G_0 - \Delta\nu$ correlations, which respectively are used to generate spatially resolved pore size distributions and degree of heterogeneity indications.

2. Materials and methods

2.1. Materials

Four different samples were investigated in this study. Sample 1 consisted of glass spheres with a diameter range of 5–50 µm (Thermo Scientific) while sample 2 consisted of glass spheres with a diameter range of 140–165 µm (Duke Scientific Corp). Sample 3 consisted of two layers with different diameter ranges horizontally divided. The bottom layer contained the 140–165 µm glass spheres and the top layer contained the 5–50 µm glass spheres. All three porous samples were saturated with distilled water. Sample 4 was a liquid sample containing a layer of light mineral oil (Sigma Aldrich) and a layer of distilled water, horizontally divided by the oil–water meniscus. The slice selective sequence (Fig. 1), referred to as sequence 1, was applied to all four samples. However, sample 4 was exclusively used for validation of the slice selection. The previously published [8] non selective pulse sequence, referred to as sequence 2, was applied to samples 1 and 2 for comparisons to the results from sequence 1. The three porous samples were prepared in glass tubes with an outer diameter of 25 mm and were 100% water saturated in a vacuum chamber.

2.2. Method

All NMR experiments were conducted on a Bruker Ascend 500 MHz vertical wide bore spectrometer with a commercial Bruker MicWB40 micro imaging probe. The pulse sequence featured in this paper (sequence 1) is shown schematically in Fig. 1 and is a slice selective version of previous work (sequence 2) published by our research group [8]. The $\frac{\pi}{2}$ and π hard pulses were calibrated to be 44 and 88 µs respectively. G_0^2D is encoded during the time T, where the number n, hard π pulses is varied from 32 to 1 in 32 steps. The decoding time T, is kept constant at 20 ms which means that the time τ' is varied from 0.2685 ms to 9.956 ms as the sequence progresses from 32 to 1 hard π pulses. The number of points (td) in the acquisitions was 2048 with a dwell time (dw) of 5 µs.

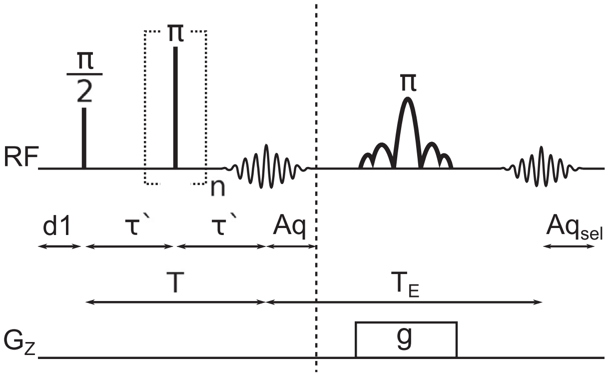

Fig. 1. Pulse sequence (sequence 1) for obtaining spatially resolved correlations between the internal gradient term G_0^2D and either magnetic susceptibility difference $\Delta\chi_{app}$ or frequency $\Delta\nu$. The non spatially resolved version (sequence 2) ends at the dotted line.

The relaxation delay was set to 10 s to ensure full longitudinal relaxation between each acquisition. In sequence 1 the second half of the echo that is refocused by the slice selective π pulse is acquired. In the non spatially resolved version (sequence 2) the second half of the echo occurring after the decoding time T, is acquired (Fig. 1). The gradient strength during the slice selective π pulse was set to $1.4797 * 10^{-4}$ T/m. The slice selective π pulse is a 3 lobe sinc pulse with pulse length = 719 µs, bandwidth = 6300 Hz and pulse power = 4.9 W. These parameters ensures slices with a thickness of 1 mm.

The slice positioning was achieved by varying the center frequency of the slice selective π pulse while keeping all other parameters constant. To probe the geometry of the 5–50 µm glass sphere layer the slice selective π pulse had an offset of −25,200 Hz. This results in a 4 mm upward displacement and this is depicted as a blue slice in Fig. 2. To probe the geometry of the 140–165 µm glass sphere layer the slice selective π pulse had an offset of +25,200 Hz, which results in a 4 mm downward displacement, depicted as a red slice in Fig. 2.

The resulting datasets from sequence 1 and 2 are matrices with FID decay throughout the rows and G_0^2D weighted decay down the columns. $\Delta\chi_{app}$ distributions were generated from 1D Inverse Laplace Transform (ILT) of the first row of the dataset and using Eq. (1). G_0 distributions were generated from 1D ILT of the first column of the datasets and the diffusion constant for water at 25 °C ($D_{H_2O} = 2.3 \cdot 10^{-5}$ cm^2/s).

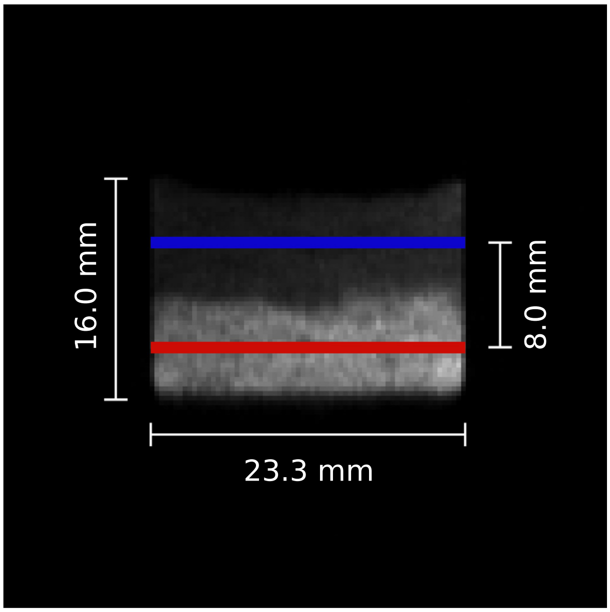

Fig. 2. Magnetic resonance image (MRI) of sample 3 demonstrating the slice position in either the 5–50 µm (blue) or the 140–165 µm (red) layer. The image was recoded in ParaVision using a spin echo acquisition where the echo time was 2.91 ms and the repetition time was 1 s. (For interpretation of the references to colour in this figure legend, the reader is referred to the web version of this article.)

The liquid dynamics in porous samples are restricted by the pore matrix. Hürlimann [1] showed that there are three length scales that are affecting the diffusion term involved with the echo attenuation of the transverse magnetization for a CPMG experiment with n echoes and a constant internal gradient G_0, (Eq. (3)).

$$\frac{M(t_E)}{M(t_E=0)} = e^{-t_E\rho_2\frac{S}{V}-\frac{1}{12}D\gamma^2G_0^2t_E^3} \tag{3}$$

The distance the molecules have to travel in order to dephase 2π radians is called the dephasing length l_g, defined as $l_g = (\frac{2\pi D}{\gamma G_0})^{\frac{1}{3}}$. The diffusion length l_D, is the length a molecule travels due to diffusion during the echo time t_E, defined as $l_D = (Dt_E)^{\frac{1}{2}}$. The final length scale is the structural length l_s, which in our case is the pore length $l_s = a$ [17,16].

If the pore length l_s is the shortest length scale i.e. $l_s \ll l_g$ and l_D, the system will be in the Motional Averaging (MAV) regime. In the MAV regime, the $\Delta\chi_{app}B_0$ term is low and the pore size is typically small. The short pore length means that the diffusing molecules will hit the walls of the pore before complete dephasing during the echo time t_E [16–18]. As the experiments featured in this paper are performed with a relatively high B_0 value and relatively large pore sizes, the MAV regime is not likely to be encountered.

If l_g is the shortest length scale i.e. $l_g \ll l_D$ and l_s, the Localization (LOC) regime applies. In the LOC regime, the $\Delta\chi_{app}B_0$ term is large and the dephasing length l_g, may be very short. Large echo attenuation is observed in such systems, as only the molecules located at a distance of l_g or less from the pore wall will contribute to the echo [16,19,17].

If the diffusion length l_D, is the shortest length scale i.e. $l_D \ll l_g$ and l_s, the system is in the Free Diffusion (FD) regime. The FD regime is valid for samples with large pores where most molecules never experience the pore walls. In this regime, one can expect a moderate internal gradient G_0, during the echo time t_E, and a small echo attenuation [16,17,20]. Because of the high $\Delta\chi_{app}B_0$ value associated with the high B_0 value in our experiments, the water molecules in all our samples are most likely subjected to a regime somewhere in the middle of the FD and the LOC regime during a spin echo acquisition.

Mitchell et al. [21,22] have developed a method for analysing CPMG data in inter-regimental systems. In this method, Eq. (3) is expressed in a general form (Eq. (4)) where b is a constant that describes decay due to diffusion in internal gradient and k describes how the diffusion exponent depends on the echo time.

$$\frac{M(nt_E)}{M(t_E=0)} = e^{-nt_E\rho_2\frac{S}{V}-bnt_E^k} \tag{4}$$

To obtain the true k value, separate CPMG measurements, where the echo time was varied from 0.2 to 3.2 ms, were performed on sample 1 and 2. The resulting diffusion decay was analysed according to Eq. (4) and the data collapse plot according to Hürlimann [1]. As seen in Fig. 3, the optimal k value was determined to be 1.95 and 2.15 for sample 1 and 2 respectively, which indicates that both samples are in between the FD ($k = 3$) and the LOC ($k = 1$) regime.

In Eq. (2), true G_0 assumes that the system occupies the FD regime [16,23]. In our analysis the FD regime was assumed, where $b = \frac{1}{12}D\gamma^2G_0^2$ and $k = 3$, even though both water saturated glass sphere environments exhibits dynamic behaviour from both the FD and LOC regime. Analysis according to the MAV and LOC regime is not performed in this paper, although influences from the LOC regime is discussed later.

To create $G_0 - \Delta\chi_{app}$ correlations the obtained data was analysed as a 2D Fredholm integral according to Eq. (5), where $t_{FID} = td \cdot dw$.

$$M(\tau', t_{FID}) = \iint P(b, T_2^*)e^{-bn\tau'^3}e^{-\frac{t_{FID}}{T_2^*}}dbdT_2^* \tag{5}$$

$G_0 - \Delta\chi_{app}$ correlations were obtained from $P(b, T_2^*)$, where $G_0 = \sqrt{\frac{12b}{D\gamma^2}}$ and $\Delta\chi = \frac{2}{\gamma B_0 T_2^*}$, after a 2D ILT of the obtained data. Pore size distributions were obtained from the measured correlations between G_0 and $\Delta\chi_{app}$ using Eq. (2). To obtain $G_0 - \Delta\nu$ correlations, the data was expressed as a combined ILT and Fourier Transform integral [14] according to Eq. (6).

$$\frac{M(t_\nu, \tau')}{M(0)} = \iint P(\nu, b)e^{-bn\tau^3}e^{-i\Delta\nu t_\nu}d\nu db \tag{6}$$

Each of the FIDs were Fourier Transformed. The resulting spectra were divided into 32 frequency intervals and 1D ILT was performed on each interval. Assuming the FD regime, as described above, this produces a G_0 distribution for each frequency interval. By assembling all G_0 distributions, a correlation plot between G_0 and $\Delta\nu$ was obtained [15]. All ILT analysis were performed using a software package [24] based on the Schlumberger algorithm [25].

3. Results and discussion

The efficiency of the slice selection was tested by applying sequence 1 to sample 4 (water and a light mineral oil horizontally separated). Fig. 4 A shows a spectrum, acquired with a non spatially resolved one pulse experiment ($\pi/2$-pulse – acquisition) on the liquid water/oil sample, containing both peaks. When the slice selective π pulse is introduced however, only one of the peaks is visible, where each one depends on the center frequency of the slice selective π pulse (Fig. 4B and C). Fig. 4 therefore shows that the slice selection is able to distinguish between water and oil in a two phase liquid sample.

In this paper results from samples 1 and 2 (acquired with both sequence 1 and 2) are compared to results from sample 3 (acquired with sequence 1). Sequence 1 and 2 are applied to sample 1 and 2 to show the effect of introducing a slice selective π pulse while keeping the sample matrix constant and thus eliminating the uncertainty associated with possible variations in packing between samples [26]. Sequence 1 is applied to sample 3 (top layer containing the 5–50 μm glass spheres and bottom layer containing the 140–165 μm glass spheres) to show that the slice selective sequence works in a sample with a heterogeneous geometry.

Lengthening a pulse sequence by increasing the total time from excitation to acquisition may cause significant signal loss. Fig. 5 demonstrates the signal loss associated with the 20 ms decoding time T, present in sequence 1 (in sample 1, 2 and 3) and 2 (in sample 1 and 2) compared to a one pulse ($\pi/2$-pulse – acquisition) experiment. The loss of signal during sequence 1 and 2 is significant compared to the one pulse experiment and predominant in the 5–50 μm glass spheres (Fig. 5A). However, the signal loss associated with the addition of the slice selective pulse in sequence 1 is insignificant as this only increases the total length of the sequence by 770 μs compared to sequence 2.

Fig. 6 shows how the distribution of $\Delta\chi_{app}$ is affected when the length of the pulse sequence is varied from a regular one pulse ($\pi/2$-pulse – acquisition) experiment, to sequence 1 and sequence 2 for both the 5–50 μm (Fig. 6 A) and the 140–165 μm (Fig. 6 B) glass spheres.

It is apparent from Fig. 6 that the 20 ms decoding time T, present in both sequence 1 and 2, is responsible for the loss of higher value $\Delta\chi_{app}$ contributions which are present in the distributions from the one pulse ($\pi/2$-pulse - acquisition) experiment. This effect is evident for both the 5–50 μm (Fig. 6A) and the 140–165

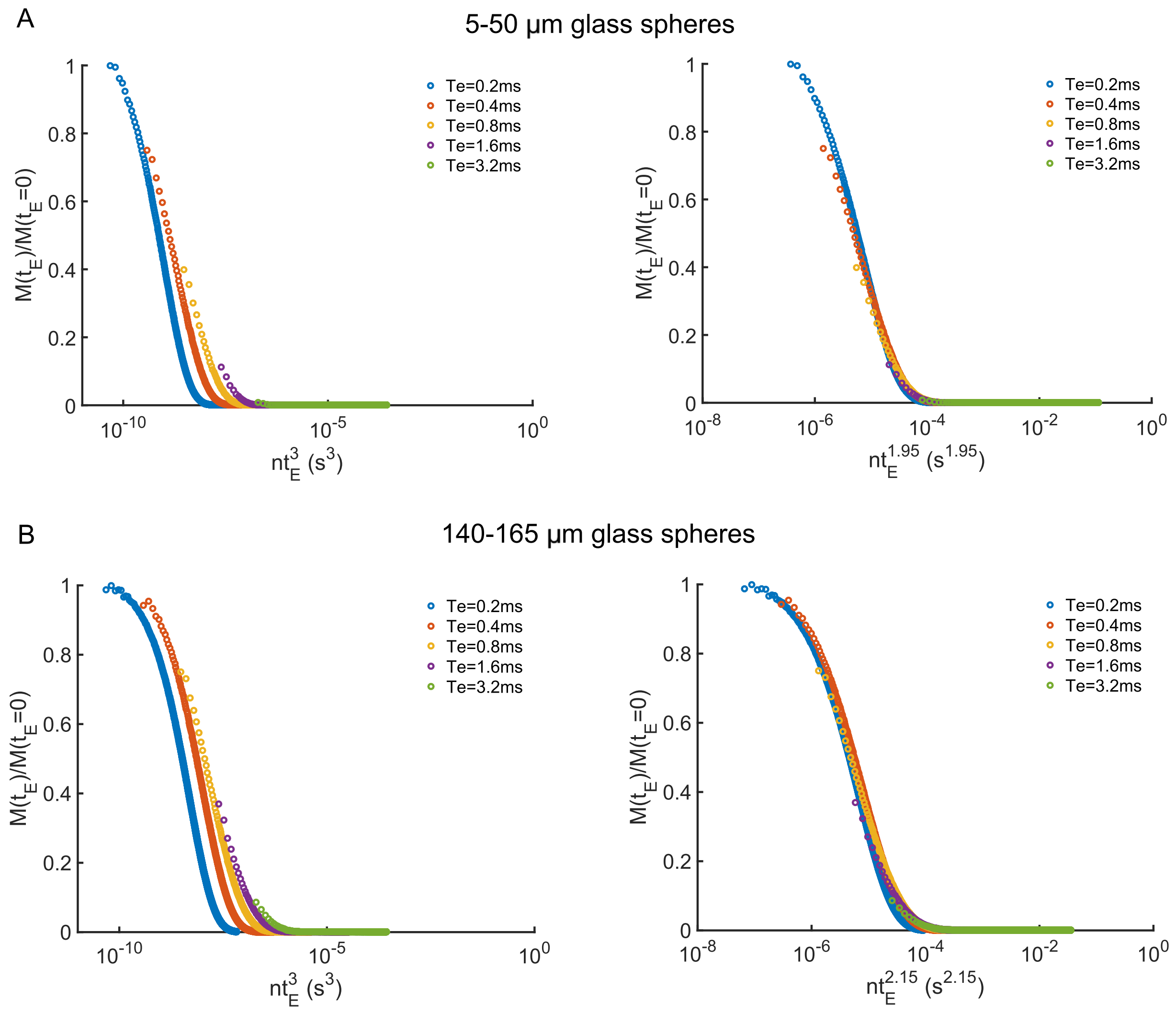

Fig. 3. Normalized diffusion decay plots from CPMG measurements where the echo time is varied from 200 µs to 3.2 ms in samples 1 (A) and 2 (B). The decay curves are plotted according to Eq. (4) with k = 3 (the free diffusion regime) and the optimal *k* value that leads to the data collapse.

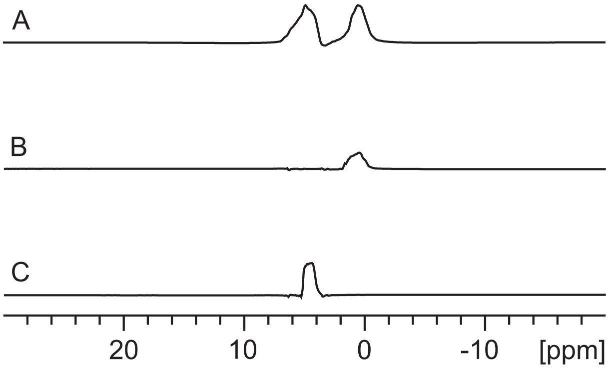

Fig. 4. Spectra, with and without slice selection recorded on a liquid sample containing water and a light mineral oil separated by a meniscus. Without slice selection the spectra contains both the water (most downfield) and the oil (most upfield) signal (A). A −25,200 Hz offset in the center frequency of the slice selective π pulse results in a slice located 4 mm above the iso centre and thus in the oil layer (B). A +25200 Hz offset in the center frequency of the slice selective π pulse results in a slice located 4 mm below the iso centre and thus in the water layer (C).

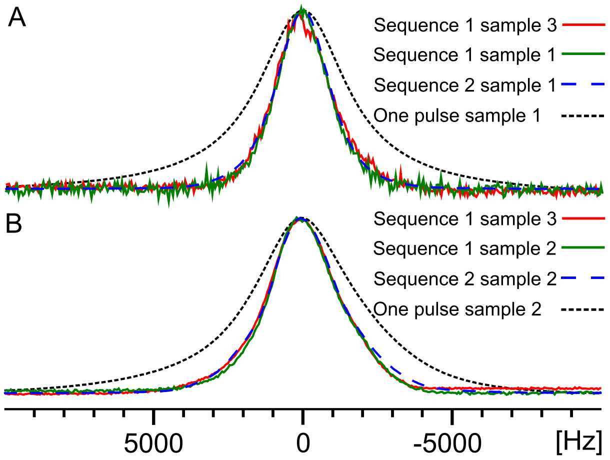

Fig. 5. Spectra from sequence 1 (in sample 1, 2 and 3) and 2 (in sample 1 and 2), obtained from row 1 in the acquired datasets (32 hard π pulses during the 20 ms decoding time T), compared to the spectrum from a regular one pulse ($\pi/2$-pulse – acquisition) experiment acquired in the water saturated 5–50 µm (A) and 140–165 µm (B) glass spheres.

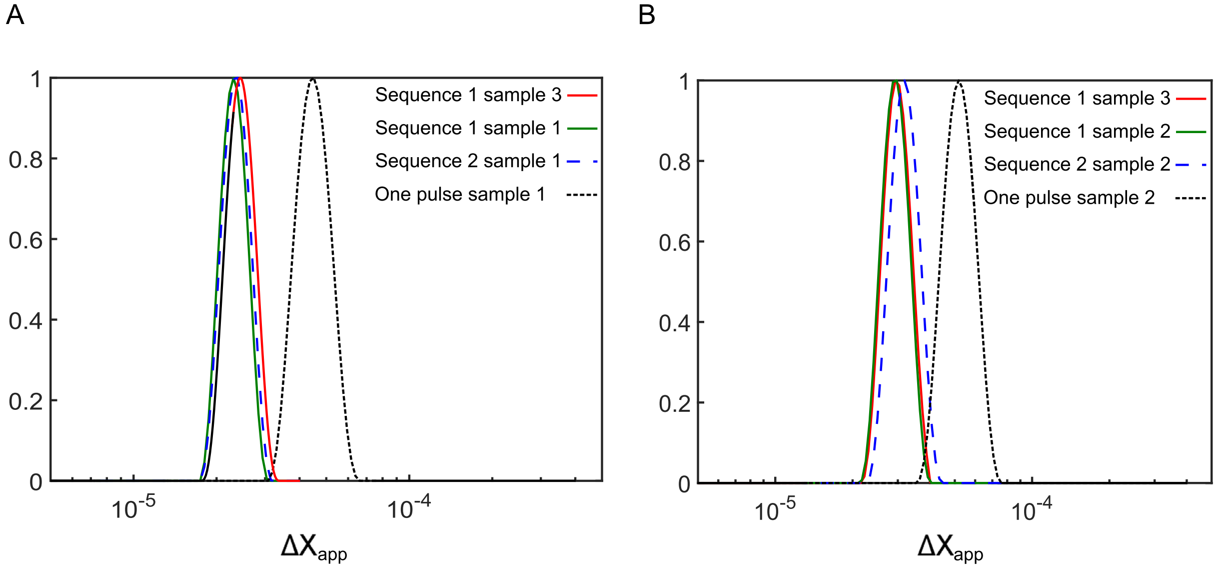

Fig. 6. $\Delta\chi_{app}$, distributions from sequence 1 (in sample 1, 2 and 3) and 2 (in sample 1 and 2), obtained from row 1 of the acquired datasets (32 hard π pulses during the 20 ms decoding time T), compared to the $\Delta\chi_{app}$ distribution from a regular one pulse (π/2-pulse – acquisition) experiment acquired in the water saturated 5–50 μm (A) and 140–165 μm (B) glass spheres. The distributions are normalized and obtained from 1D ILT of the FIDs and Eq. (1).

μm (Fig. 6B) glass spheres. However, as for the signal loss seen in the spectra shown in Fig. 5, the loss of high value $\Delta\chi_{app}$ contributions (Fig. 6) is predominant in the 5–50 μm glass spheres. Some additional loss of higher value $\Delta\chi_{app}$ contributions was expected for the marginally longer (770 μs) sequence 1, compared to sequence 2. This was seen within sample 1 and 2 for both glass sphere environments. However, the results from sample 3 show that the $\Delta\chi_{app}$ distribution from the top layer of sample 3 have marginally higher $\Delta\chi_{app}$ values than the $\Delta\chi_{app}$ distributions from sample 1 (Fig. 6A). This suggests that the packing of the 5–50 μm glass spheres in the top layer of sample 3 might be slightly different than the packing of the 5–50 μm glass spheres in sample 1. The $\Delta\chi_{app}$ distribution from the bottom layer of sample 3 (sequence 1) was however, close to identical to the one acquired with sequence 1 in sample 2, meaning that the difference in packing of the 140–165 μm glass spheres seems to be insignificant (Fig. 6B).

In Fig. 7, the internal gradient G_0 distributions for the 5–50 μm and 140–165 μm glass spheres are shown for both sequence 1 and 2. In the 5–50 μm glass spheres (Fig. 7A) higher G_0 contributions are lost in sequence 1 (in both sample 1 and 3) compared to sequence 2 (in sample 1). As G_0 is inversely proportional to pore size (Eq. (2)), this effect will cause a bias towards larger pore sizes. The G_0 distributions created from sequence 1 (red and green[1] lines in Fig. 7A) are very similar and the minor differences can be attributed to local variations in the glass sphere packing between sample 1 and 3. On the low G_0 value end, the distributions from all three acquisitions are similar.

In the high value end of the G_0 distributions obtained in the 140–165 μm glass spheres (Fig. 7B), all three G_0 distributions are similar. In the low value end however, the G_0 distribution from sequence 1 (in both sample 2 and 3) have consistently lower values. This effect will also cause a bias towards larger pore sizes.

Fig. 8 shows the $G_0 - \Delta\chi_{app}$ correlation plots from the 5–50 μm (Fig. 8A) and the 140–165 μm (Fig. 8B) glass spheres. For both glass sphere environments, there seems to be a marginal loss in the range of both $\Delta\chi_{app}$ and G_0 between sequence 1 and 2 within samples 1 and 2. This was also observed in Figs. 6 and 7 respectively. There are also small deviations in the correlation plots acquired using sequence 1 in the top layer of sample 3 and the correlation plots acquired using sequence 1 in sample 1. These small deviations are attributed to the difference in packing of the 5–50 μm glass spheres. The correlation plots acquired using sequence 1 in the bottom layer of sample 3 and the ones acquired using sequence 1 in sample 2 are almost identical, which again suggests that the difference in packing is less of a factor in the 140–165 μm glass spheres.

The correlation plots, shown in Fig. 8, can be used as an indication of difference in average pore size between samples. When comparing the correlation slopes from both glass sphere environments one can see that the slopes from the 5–50 μm glass spheres are generally steeper than their counterpart in the 140–165 μm glass spheres. This is reasonable as the $G_0 - \Delta\chi_{app}$ correlation slope is given by B_0/a (Eq. (2)), where a is the pore diameter, meaning that the slope is inversely proportional to pore size and one can thus immediately identify which sample has the coarsest grains. It is also worth mentioning that any deviation from linearity in the slope may be an additional indication of grain heterogeneity, although this must be further researched.

Fig. 9 shows the resulting pore size distributions. In Fig. 9 A the pore size distributions calculated from $G_0 - \Delta\chi_{app}$ correlations obtained from sequence 1, in both sample 1 and the top layer of sample 3, are shown and compared to results from sample 1 generated by sequence 2 and the DDIF method. In Fig. 9B the pore size distributions calculated from $G_0 - \Delta\chi_{app}$ correlations obtained from sequence 1, in both sample 2 and the bottom layer of sample 3, are shown and compared to results from sample 2 generated by sequence 2 and the DDIF method. In the DDIF method, t_e was 150 μs and the t_d was logarithmically varied from 1 ms to 15 s. A comparison to DDIF is provided for both glass sphere environments. However, the maximum detectable pore size using the DDIF method in water saturated samples is approximately 100 μm, limited by the relaxation time [10]. The 140–165 μm glass spheres might have pores larger than 100 μm so the DDIF method should therefore be most accurate in the 5–50 μm glass spheres.

When comparing the pore size distributions created from pulse sequence 1 and 2, the distributions created from sequence 1, in

---

[1] For interpretation of color in Fig. 7, the reader is referred to the web version of this article.

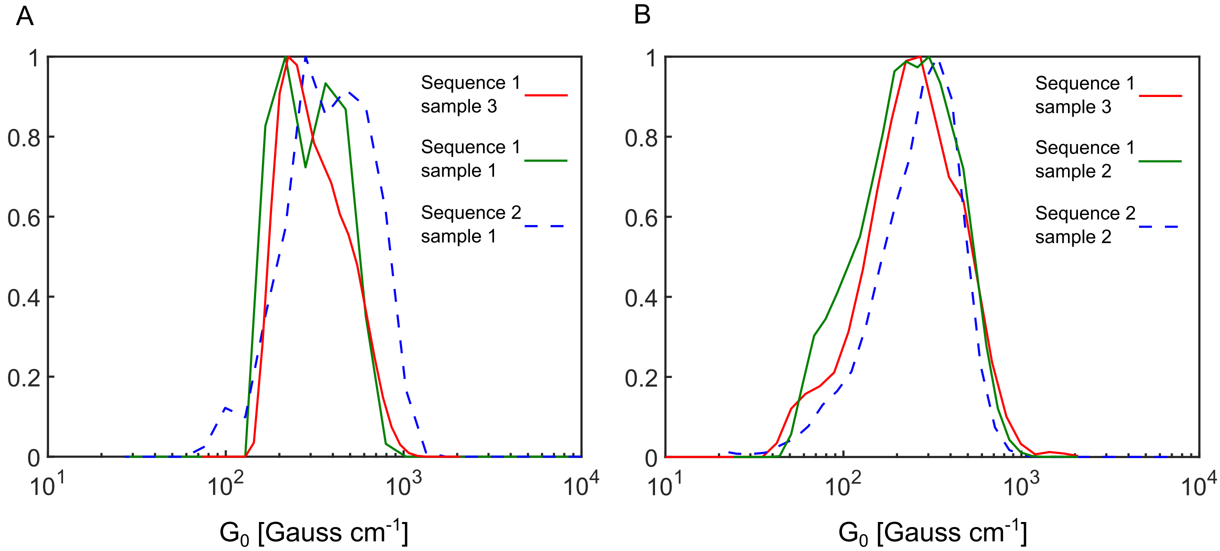

Fig. 7. Internal gradient G_0, distributions from sequence 1 (in sample 1, 2 and 3) and 2 (in sample 1 and 2), acquired in the water saturated 5–50 µm (A) and 140–165 µm (B) glass spheres. The distributions are normalized and were obtained from 1D ILT of the first column of the acquired datasets.

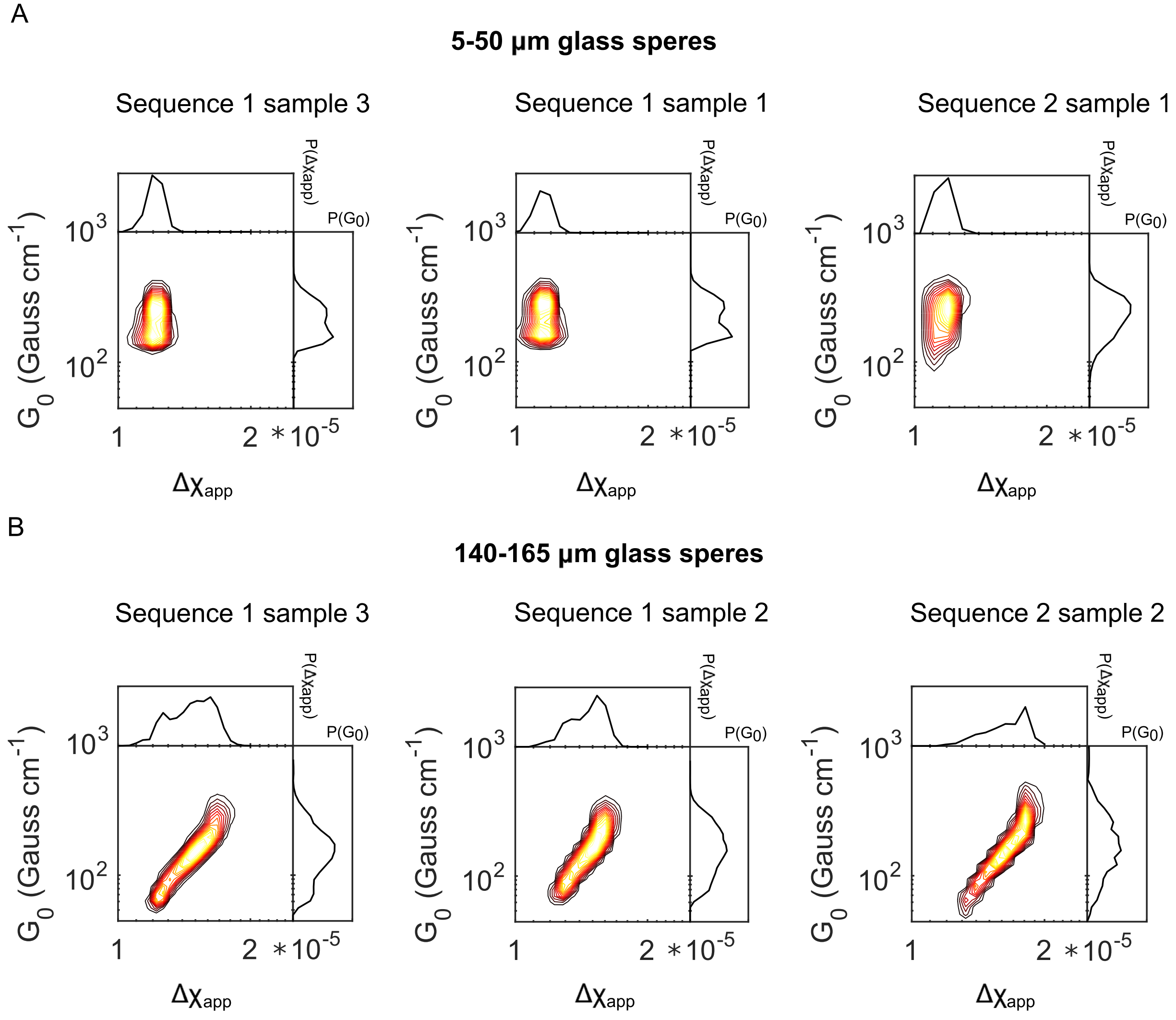

Fig. 8. $G_0 - \Delta\chi_{app}$ correlations from water saturated 5–50 µm (A) and 140–165 µm (B) glass spheres obtained from sequence 1 (in sample 1, 2 and 3) and sequence 2 (in sample 1 and 2).

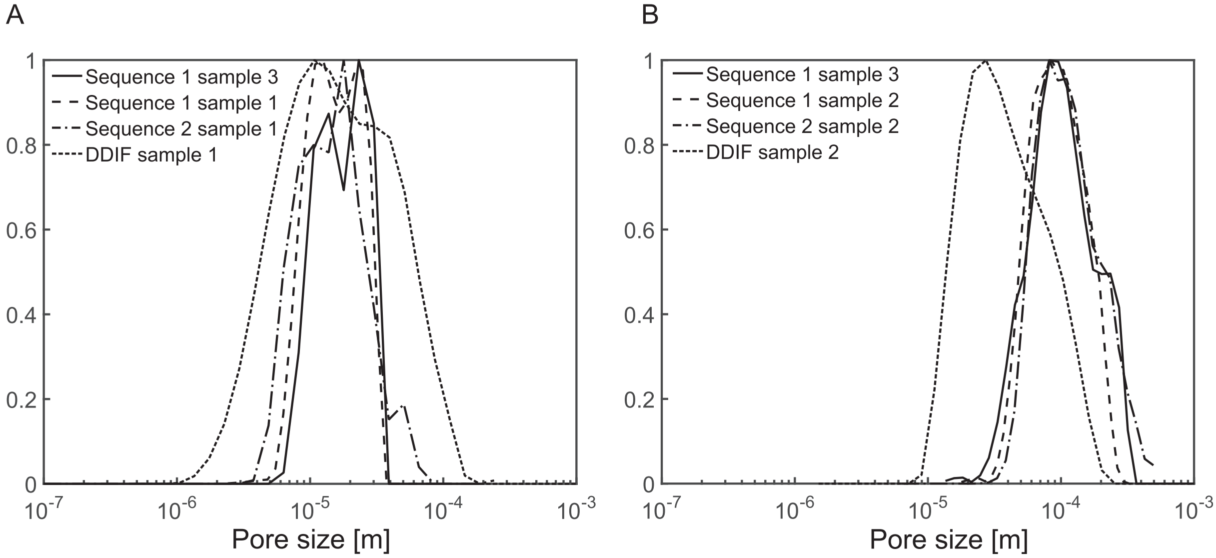

Fig. 9. Pore size distributions from the 5–50 μm glass spheres (A) and the 140–165 μm glass spheres (B) obtained from slice selective and non slice selective $G_0 - \Delta\chi_{app}$ correlations (sequence 1 and 2) as well as the DDIF method.

both sample 1 and 3 (top layer) seem to consistently omit the smallest pores in the 5–50 μm glass spheres (Fig. 9A). This is consistent with the loss of higher G_0 values, seen in Fig. 7A. The highest G_0 values originates from the smallest pores, which means that a loss in high G_0 values may also remove the smallest pores from the pore size distribution. Still, the median values from both of the selective as well as the non selective pore size distributions are approximately 20 μm. This is a reasonable value for the 5–50 μm glass spheres and is in good agreement with the median value from the DDIF method and from previous experiments with the same glass spheres [8]. In the 5–50 μm glass spheres, the DDIF method yielded a pore size ranging from 1 μm to 200 μm while sequence 1 and 2 produced ranges of 3 μm to 40 μm and 3 μm to 100 μm respectively. Since the largest glass spheres have a

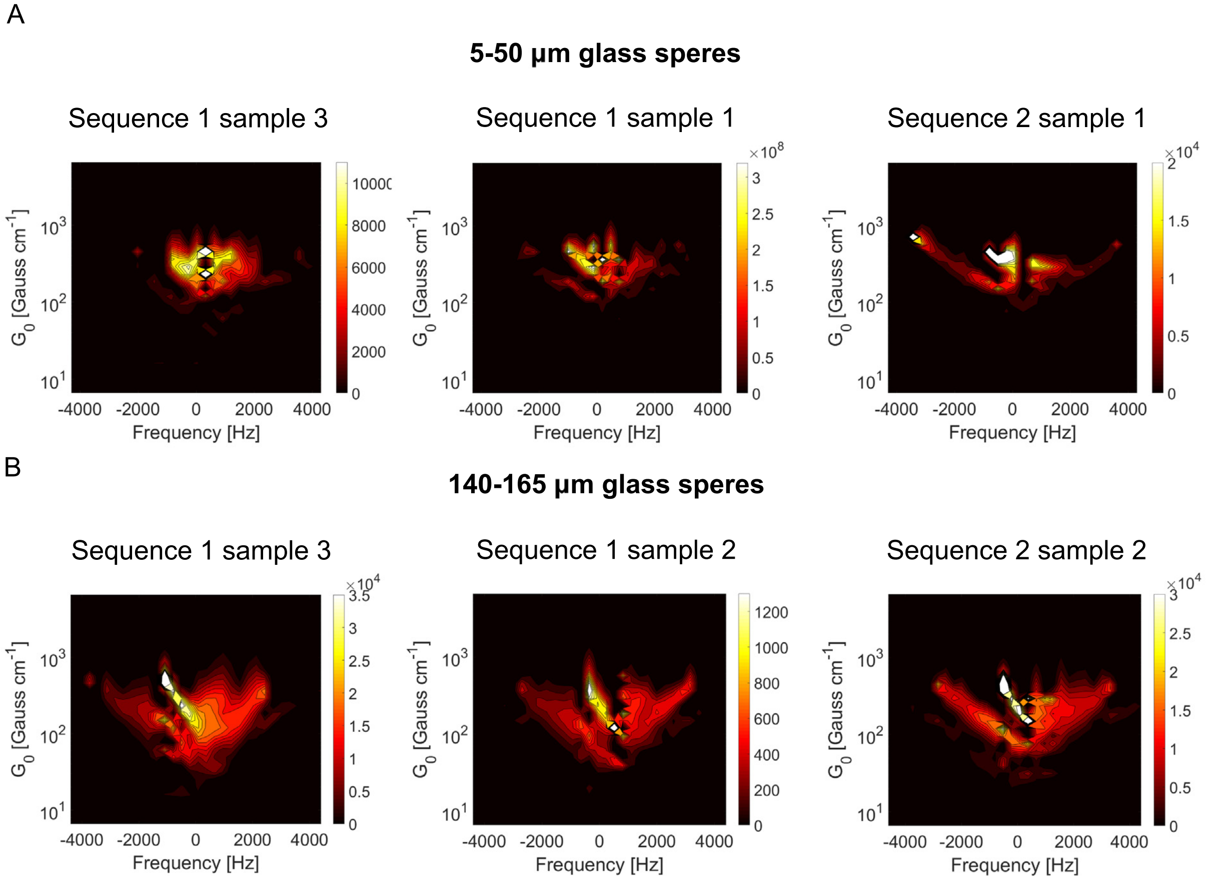

Fig. 10. $G_0 - \Delta\nu$ correlations from water saturated 5–50 μm (A) and 140–165 μm (B) glass spheres obtained from sequence 1 (in sample 1, 2 and 3) and 2 (in sample 1 and 2).

diameter of 50 μm, sequence 1 produced the most correct pore size range.

Fig. 9B shows a very good agreement between the pore size distributions from sequence 1 and sequence 2 in the 140–165 μm glass spheres regardless of sample. The marginal differences in $\Delta\chi_{app}$ (Fig. 6 B) and G_0 Fig. 7B) between the two methods does not seem to significantly affect the resulting pore size distributions. The good agreement between the two samples suggests that the packing of the 140–165 μm glass spheres was similar in samples 2 and 3. Compared to the 5–50 μm glass spheres, the particle size is more homogeneous in the 140–165 μm glass spheres, which means that packing related uncertainty becomes less of a factor in the 140–165 μm glass spheres.

All three distributions created from $G_0 - \Delta\chi_{app}$ correlations have a median value of approximately 100 μm, while the DDIF method provides a median value of approximately 40 μm. In the 140–165 glass spheres, the pore size distribution should have a median value of approximately 70 [27], meaning that the true pore size distribution lies somewhere between the distributions from the $G_0 - \Delta\chi_{app}$ correlations and the one from the DDIF method. In our method, based on $G_0 - \Delta\chi_{app}$ correlations, we assume that G_0 is constant across the length of a pore. In samples, where the pore size is large compared to the diffusion length, the molecules will not experience an average (constant) gradient. The molecules will then be more sensitive to local gradients which varies on a considerably smaller scale than the pore length. Molecules positioned in the middle of the pore, will then experience a gradient that is weaker than the average value across the pore. This effect will lead to an underestimation of G_0 and since G_0 is inversely proportional to the pore size, it will lead to an overestimation of the pore size. Further work should include repetition of these experiments at lower magnetic field strengths to ensure the FD regime and exclude disturbances from molecules in the LOC regime.

Fig. 10 shows the $G_0 - \Delta v$ correlations for both the 5–50 μm and the 140–165 μm glass spheres obtained from sequence 1 and 2 (in sample 1, 2 and 3). Burcaw and Callahan [14] suggested that correlations between high G_0 values and high absolute values of frequency are indications of homogeneous samples while a more full G_0 range at all frequencies indicates heterogeneity. The correlation between high G_0 values and high absolute values of frequency, seen in homogeneous samples, should amount to a pattern resembling butterfly wings. A butterfly pattern in the $G_0 - \Delta v$ correlation plot indicates a higher degree of homogeneity and these plots can thus be used to determine which of two samples has the most homogeneous/heterogeneous particle size range. In the $G_0 - \Delta v$ correlation plots, the butterfly pattern is more predominant for the 140–165 glass spheres (Fig. 10B). This suggest a higher degree of homogeneity in the 140–165 μm glass spheres, compared to the 5–50 μm glass spheres (Fig. 10A), which is reasonable as the 140–165 μm glass spheres has the most narrow particle size range. It is however, worth mentioning that a similar correlation between high G_0 values and high absolute values of frequency was also observed in the $G_0 - \Delta v$ correlation obtained from sequence 2 in the 5–50 μm glass spheres.

4. Conclusions

Spatially resolved pore size distributions and $G_0 - \Delta v$ correlation maps based on $G_0 - \Delta\chi_{app}$ correlations were successfully created with a slice selective 2D pulse sequence (sequence 1) in both 5–50 μm and 140–165 μm water saturated glass spheres. The results from sequence 1 were compared to results from non spatially resolved $G_0 - \Delta\chi_{app}$ correlations (sequence 2) performed on the same sample to eliminate the uncertainty associated with glass sphere packing. Sequence 1 was additionally applied to a separate two layer sample (sample 3) and the results from both layers were presented as well.

In sample 1 (5–50 μm glass spheres) there is a decent agreement between pore size distributions from sequence 1 and 2. The minor deviation between sequence 1 and 2 was attributed to loss of high value G_0 contributions in sequence 1 caused by the marginally longer length (+770 μs) of this sequence. This effect is only an issue for very small particle environments as it does not manifest itself in the 140–165 μm glass spheres. The distribution acquired using sequence 1 in the top layer (5–50 μm glass spheres) of sample 3 is also in decent agreement with the results from sample 1. The minor deviations between the results from sequence 1 in sample 1 and 3 are attributed to minor differences in glass sphere packing. All three pore size distributions produced a reasonable median value in the 5–50 μm glass spheres.

In sample 2 (140–165 μm glass spheres) the pore size distributions from sequence 1 and 2 are almost identical. The distribution acquired using sequence 1 in the bottom layer (140–165 μm glass spheres) of sample 3 is also in good agreement with the results from sample 2. This suggests that glass sphere packing is less of a factor in the 140–165 μm glass spheres. However, all three pore size distributions from the 140–165 μm glass spheres overestimated the pore size by small margin.

$G_0 - \Delta v$ correlation maps were presented and these maps correctly indicated a slightly higher degree of homogeneity in the 140–165 μm glass spheres. Such maps can thus be used to decide which of two samples have the most homogeneous/heterogeneous particle size. As an addition to pore size distributions, spatially resolved $G_0 - \Delta v$ correlations may be useful as an indication of heterogeneity.

At the magnetic field strength featured in this paper, the water molecules in both glass sphere environments were subject to a mixture of the LOC and the FD regime. Further work should include repetition of these experiment in low field NMR to ensure the FD regime.

Acknowledgements

The authors acknowledge The Research Council of Norway for support through the Norwegian NMR Platform, NNP (226244/F50) and Equinor ASA for funding the project “Wetting in porous media” through AKADEMIA.

References

[1] M.D. Hürlimann, Effective gradients in porous media due to susceptibility differences, J. Magn. Reson. 131 (2) (1998) 232–240.
[2] B. Sun, K.J. Dunn, Probing the internal field gradients of porous media, Phys. Rev. E 65 (2002) 1–7.
[3] Y. Zhang, B. Blümich, $g_{int}^2 d - t_2$ correlation nmr of porous media, J. Magn. Reson. 252 (2015) 176–186.
[4] J. Kärger, H. Pfeifer, S. Rudtsch, The influence of internal magnetic field gradients on nmr self-diffusion measurements of molecules adsorbed on microporous crystallites, J. Magn. Reson. (1969) 85 (2) (1989) 381–387.
[5] Q. Chen, A.E. Marble, B.G. Colpitts, B.J. Balcom, The internal magnetic field distribution, and single exponential magnetic resonance free induction decay, in rocks, J. Magn. Reson. 175 (2) (2005) 300–308.
[6] P.M. Singer, G. Leu, E.J. Fordham, P.N. Sen, Low magnetic fields for flow propagators in permeable rocks, J. Magn. Reson. 183 (2) (2006) 167–177.
[7] D. Bernin, D. Topgaard, Nmr diffusion and relaxation correlation methods: new insights in heterogeneous materials, Curr. Opin. Colloid Interface Sci. 18 (3) (2013) 166–172.
[8] R.T. Lewis, J.G. Seland, Characterization of pore geometry using correlations between magnetic field and internal gradient, Micropor. Mesopor. Mater. 269 (2018) 31–34.
[9] J. Mitchell, Rapid measurements of heterogeneity in sandstones using low-field nuclear magnetic resonance, J. Magn. Reson. 240 (2014) 52–60.
[10] Y.-Q. Song, Determining pore sizes using an internal magnetic field, J. Magn. Reson. 143 (2) (2000) 397–401.
[11] Y. Zhang, L. Xiao, G. Liao, Spatially resolved pore-size - t2 correlations for low-field nmr, Micropor. Mesopor. Mater. 269 (2018) 142–147.

[12] A. Sodickson, D.G. Cory, A generalized k-space formalism for treating the spatial aspects of a variety of nmr experiments, Prog. Nucl. Magn. Reson. Spectrosc. 33 (2) (1998) 77–108.

[13] B. Audoly, P. Sen, S. Ryu, Y.-Q. Song, Correlation functions for inhomogeneous magnetic field in random media with application to a dense random pack of spheres, J. Magn. Reson. 164 (1) (2003) 154–159.

[14] L.M. Burcaw, P.T. Callaghan, Correlation of the inhomogeneous field as a measure of sample heterogeneity, J. Magn. Reson. 216 (2012) 144–151.

[15] J.G. Seland, Dynamic correlations between inhomogeneous magnetic fields, internal gradients, diffusion and transverse relaxation, as a probe for pore geometry and heterogeneity, diffusion-fundamentals.org 22 (10) (2014) 1–5.

[16] J. Mitchell, T.C. Chandrasekera, M.L. Johns, L.F. Gladden, E.J. Fordham, Nuclear magnetic resonance relaxation and diffusion in the presence of internal gradients: the effect of magnetic field strength, Phys. Rev. E 81 (2010) 026101.

[17] R.T. Lewis, J.G. Seland, A multi-dimensional experiment for characterization of pore structure heterogeneity using nmr, J. Magn. Reson. 263 (2016) 19–32.

[18] M. Hurlimann, K. Helmer, T. Deswiet, P. Sen, Spin echoes in a constant gradient and in the presence of simple restriction.

[19] T.M. de Swiet, P.N. Sen, Decay of nuclear magnetization by bounded diffusion in a constant field gradient, J. Chem. Phys. 100 (8) (1994) 5597–5604.

[20] P. Le Doussal, P.N. Sen, Decay of nuclear magnetization by diffusion in a parabolic magnetic field: an exactly solvable model, Phys. Rev. B 46 (1992) 3465–3485.

[21] J. Mitchell, T.C. Chandrasekera, L.F. Gladden, Measurement of the true transverse nuclear magnetic resonance relaxation in the presence of field gradients, J. Chem. Phys. 139 (7) (2013) 074205.

[22] J. Mitchell, T.C. Chandrasekera, Understanding generalized inversions of nuclear magnetic resonance transverse relaxation time in porous media, J. Chem. Phys. 141 (22) (2014) 224201.

[23] J. Mitchell, T.C. Chandrasekera, L.F. Gladden, Obtaining true transverse relaxation time distributions in high-field nmr measurements of saturated porous media: removing the influence of internal gradients, J. Chem. Phys. 132 (24) (2010) 244705.

[24] Provided by courtesy of Professor Paul T. Callaghan.

[25] L. Venkataramanan, Y.-Q. Song, M.D. Hurlimann, Solving fredholm integrals of the first kind with tensor product structure in 2 and 2.5 dimensions, IEEE Trans. Signal Process. 50 (5) (2002) 1017–1026.

[26] B. Brattekås, T.L. Føyen, T. Vabø, H. Haugland, S.I. Reite, A.S. Saunes, M.A. Fernø, Dos and don'ts when developing a system to investigate spontaneous imbibition in unconsolidated porous media, in: The International Symposium of the Society of Core Analysts held in Trondheim, Norway, 27–30 August 2018.

[27] G.C. Barker, A. Mehta, Vibrated powders: structure, correlations, and dynamics, Phys. Rev. A 45 (1992) 3435–3446.